Brandaris Ultra High-Speed Imaging Facility

Guillaume Lajoinie, Nico de Jong and Michel Versluis

Abstract High-speed imaging is in popular demand for a broad range of scientific applications, including fluid physics, and bubble and droplet dynamics. It allows for a detailed visualization of the event under study by acquiring a series of images captured at high temporal and spatial resolution. The challenge here is the combination of microscopic length scales and ultrashort time scales associated with the mechanisms governing fluid flows. In this chapter, ultra high-speed imaging at frame rates exceeding 10 million frames per second (fps) is briefly reviewed, including the emerging ultrafast sensor technologies and ultrashort nanoseconds flash illumination techniques. We discuss in detail the design and applications of the Brandaris 128 ultra high-speed imaging facility. The high-speed camera combines the optical frame of a rotating mirror camera with 128 CCD sensors and can record at a maximum frame rate of 25 Mfps. Six acquisitions can be stored in the on-board memory buffer, while in a segmented mode images are acquired in subsets, e.g. 24 × 32 frames, allowing parametric studies to be performed. We also discuss how the Brandaris camera is operated to capture details of bubble dynamics, droplet vaporization, and inkjet printing.

G. Lajoinie (✉) · M. Versluis
Physics of Fluids Group, University of Twente, 217 7500 AE, Enschede, The Netherlands
e-mail: g.p.r.lajoinie@utwente.nl

M. Versluis
e-mail: m.versluis@utwente.nl

N. de Jong
Department of Biomedical Engineering, Erasmus MC, Rotterdam, The Netherlands
e-mail: n.dejong@erasmusmc.nl

1   Introduction

In the last two decades high-speed imaging has emerged as an important tool for a variety of applications. These include car crash testing, air bag deployment, machine vision technology for packing and sorting, high-speed impact and material testing, sport science, ballistics and (nuclear) detonation and explosions. In fluid dynamics [1], high-speed imaging has been used in propulsion and cavitation, combustion, turbines and supersonic flows, sprays and jets, and shock waves. Emerging applications in microfluidics, biomedicine, and biomechanics require top-of-the-line high-speed imaging systems, i.e. high frame rates at high spatial resolution at a high number of frames to resolve the microscopic details at microseconds time resolution.

Digital high-speed imaging devices include specially devised charge-coupled device (CCD) and complementary metal-oxide semiconductor (CMOS) sensors. The CCD sensor is popular for its low noise characteristics and has a corresponding sensitivity coupled to the noise floor within the individual pixels. Pixels can be as small as 2.5 μm, making up a very compact chip. While CCD chips have a better image quality because of their reduced noise component, chips fabricated using CMOS technology are by far less expensive and faster and require less power to operate. Each CMOS pixel can be read out individually, and no shifting of the rows is necessary (as with CCDs), which dramatically reduces the readout time of a subframe of the chip. As also the data size extracted from the region of interest is reduced, CMOS chips allow for a much faster readout, up to 1 Mfps, before the upper limit of the throughput is reached. CMOS chips are, literally *a bit* more noisy and the pixels in CMOS high-speed imaging systems are often larger, typically of a size of 20 μm, to increase their sensitivity. For a typical microscopic applications this can be problematic as a higher magnification will be needed to obtain a similar field of view.

The interesting questions that need to be answered before we perform the actual high-speed imaging experiment are as follows. First, what is the required frame rate that we need to resolve our event. Second, what exposure time are required to reduce motion blur for example, and finally, how do frame rate and exposure time relate to the desired magnification, in other words how are the spatial sampling resolution and the temporal sampling resolution connected. For the first question, the key feature is the relevant timescale of the event. In a cyclic event with a known (driving) frequency or repetition rate, following the Nyquist sampling theorem, the required sampling rate should be more than twice, or more conveniently ten times, the cycle frequency. However, most applications are non-cyclic and the relevant timescale may not be obvious. One may suggest to use the typical velocity to estimate the relevant timescale, but the timescale also scales with the inverse length scale. Thus, the optimum frame rate f can be determined [1] from the ratio of the typical velocity V and the typical length scale ℓ, i.e. the relevant frequency or rate:

$$f = \frac{N \cdot V}{\ell} \qquad (1)$$

with N sufficiently high, but at least larger than 2, not to undersample the event under study. It is evident from Eq. 1 why high-speed imaging in microfluidic applications is important, as at microscopic level ℓ is very small and as a consequence the frame rate f needs to be large.

One example depicted in Fig. 1(left) shows the head of an ink-jet droplet shortly after ejection from a drop-on-demand micronozzle. The typical volume contained within the single microdroplets is 15 pL, which corresponds to a typical size of approximately 10 μm. The speed with which the droplets are ejected is 10 m/s. While such a velocity may seem rather non-extreme, Eq. 1 dictates that a frame rate of 10 Mfps is required to image the flight of the microdroplet because of the microscopic length scale of the problem. Another way to look at this problem is to note that the droplet flies with a speed of 10 m/s, which corresponds to 10 μm/μs. Thus, the typical timescale of a 10-μm droplet flying at 10 m/s is 1 μs, and correspondingly it needs to be captured at a fraction of a microsecond.

A second example is that of an oscillating microbubble, see Fig. 1(right). These stabilized microbubbles are used clinically as ultrasound contrast agents for ultrasound imaging for their superior echogenicity due to gas compressibility, which results in a nine orders higher acoustic scattering cross section as compared to particles of the same size. The bubbles resonate when driven near their eigenfrequency [2, 3], which leads, first, to the generation of an even stronger echo, as the bubble oscillates with higher amplitude, and, second, to the generation of harmonics, emitted at multiples of (second, third harmonic) [4, 5] and half (subharmonic) the driving frequency [6, 7]. These nonlinear features of bubble dynamics provide high contrast and allow to discriminate bubble echoes from linear tissue echoes. Blood, being a very poor ultrasound scatterer, can be seeded with an
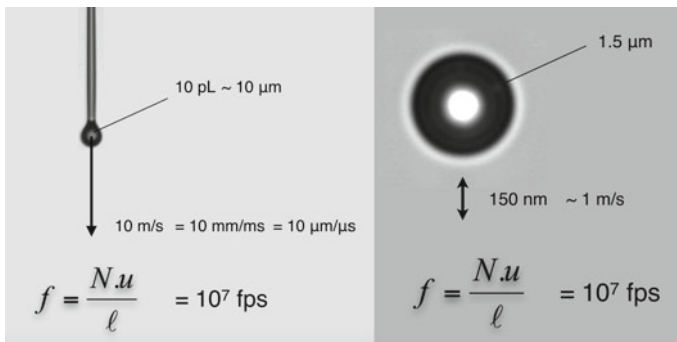
Fig. 1 Cartoon used to estimate the required frame rate for high speed imaging based on typical length scales and typical velocities. *Left* example for inkjet printing. *Right* example for an oscillating microbubble. Both examples are at microscopic scale and a simple calculation shows that ultra high-speed imaging is required at 10 Mfps

intravenous injection of ultrasound contrast microbubbles. The bubbles then act as a blood pool agent and the perfusion of organs can be visualized in real-time, as well as the hypervascularization of malignant lesions. A typical radius R of these microbubbles is 3 μm, and at frequencies near their eigenfrequency ω_0 of 1–10 MHz their oscillation amplitude is around 10% of the ambient radius. This 300-nm amplitude can be temporally resolved, based on simple arguments on a multiple of the frequency, resulting in 10 Mfps. Based on sinusoidal driving frequency $P_A \cdot \sin(\omega_0 t)$, a response of the bubble $R = R_0 + \Delta R \cdot \sin(\omega_0 t)$ a velocity of the oscillation of $\dot{R} = \omega_0 \Delta R \cdot \cos(\omega_0 t)$ with magnitude $\omega_0 \Delta R = 1$ m/s. Equation 1 then also gives 10 Mfps as the optimum frame rate.

2 Ultra High-Speed Imaging

2.1 Ultra High-Speed Imaging Camera Technology

To adequately image these event requires pushing the limits of current CCD and CMOS camera technology and perform high-speed imaging at frame rates higher than 1 Mfps with a sufficient number of frames (typically one hundred or more). We therefore need to resort to unconventional designs. The simplest solution is to follow the classic examples of using a set of multiple cameras. This principle in fact predates cinematography and was used in 1878 by Muybridge [8] in the famous first framing recording of a galloping horse, employing 12 separate cameras. Later, Brixner [9] used a similar technique with 37 cameras to record the first nuclear explosion at a 1 ms interframe time. An 8-channel image-intensified ultra high-speed framing camera for high-speed shock wave imaging was developed [10], which was later commercialized (Imacon 468). It utilizes a pyramidal beam splitter with an octagonal base that redirects the incoming image to eight individual image-intensified CCDs. Various companies now offer cameras with similar beam-splitting configurations and 1 or 2 Mpixel chip size. Some camera manufacturers use splitters for four channels equipped with color iCCDs and then split electronically the four RGGB channels to acquire 16 images at 1 Mfps. The image intensifiers used in front of the CCD sensor can be gated as short as 5 ns, leading to a frame rate as high as 200 Mfps, and very high gain levels can be applied that allow for sufficient sensitivity at such short exposure times. Another system, called the Ultranac [11] provides 24 frames at 20 Mfps by sweeping the electron beam in the intensifier. However, the image intensifiers in all these systems degrade the image quality and, as a result of the beam splitting, a high gain needs to be applied to the intensifiers, decreasing the dynamic range and increasing the noise levels. Nevertheless, these systems are unique in the 100–200 Mfps segment. A second class of imaging systems utilizes in situ storage (ISIS) of image data on the CCD chip itself. This type of sensor can record 103 frames in a single experiment at a maximum frame rate of 1 Mfps with a fixed resolution of 312 × 260 pixels. Recent

developments in CMOS technology include backside-illuminated (BSI) image sensors with increased quantum efficiency, a fill factor of nearly 100% and frame rates reaching 10–20 Mfps. For details, see Chap. 2.

In the presented cases one would like to image directly at the timescale of the event. When the timescales become as small as nanoseconds the current camera technologies present an insurmountable problem, with the exception of reproducible and repetitive events. In this special case, stroboscopic imaging can be used even without the use of (expensive) ultra-high-speed camera machinery. In stroboscopic imaging the high-speed flash photography technique is applied, and all consecutive recordings are delayed by a fixed time spacing that is tuned such that it spans the interframe time of the camera. Then, playing the captured frames in a video sequence provides us with a stroboscopic movie of the event, which in many cases cannot be distinguished from a real-time high-speed movie, and moreover with a dramatically improved spatial image resolution.

The application of flash photography in experiments is primarily aimed at obtaining precise information about the position and dimensions of the studied object at a certain instant in time. It is therefore of prime importance to capture the smallest details in both space and time with the highest contrast. To define this more quantitatively, three criteria can be defined [12]. First, based on the spatial resolution and pixel size, the spatial Nyquist criterion defines the magnification, avoiding oversampling or a too small field-of-view. Secondly, to ensure maximum image contrast, the intensity of the illumination should be adjusted to cover the full dynamic range of the camera sensor. The extent to which the intensity can be varied is, however, limited due to the reciprocal relationship between illumination intensity and exposure time. Finally, minimizing motion blur is accomplished by minimizing the temporal resolution of the imaging system. The temporal resolution is determined by the duration of the illumination pulse or by the camera exposure time; whichever is shorter defines the degree of motion blur.

Here we shorten the temporal resolution with a laser pulse to obtain nanoseconds illumination precision. Exciting a laser dye solution with a pulsed laser resulted in a short flash. The resulting high-intensity fluorescence removes the coherence of the laser light, which would lead to interference and speckle. The illumination time of the light source is only 7 ns. To record the images, a sensitive, but otherwise, standard CCD camera is used. The short illumination time of the fluorescence light source then gives the possibility to choose a time step resolution corresponding to the smallest timescale of the experiment.

As an example of the iLIF technique, Fig. 2 shows the formation of inkjet droplets captured in flight. As before, these picoliter droplets are ejected from the inkjet printhead at a speed of 10 m/s. Imaging these droplets at microscopic resolution demands a spatiotemporal resolution that cannot be provided by real-time ultra high-speed imaging, however owing to the near-perfect reproducibility of the inkjet system a the stroboscopic principle can be applied to capture these microdroplets with superior clarity. Using this method a perfect delineation of the droplet contour can be obtained, from which the one-dimensional velocity profile inside a single droplet is extracted during drop formation. To that purpose a novel
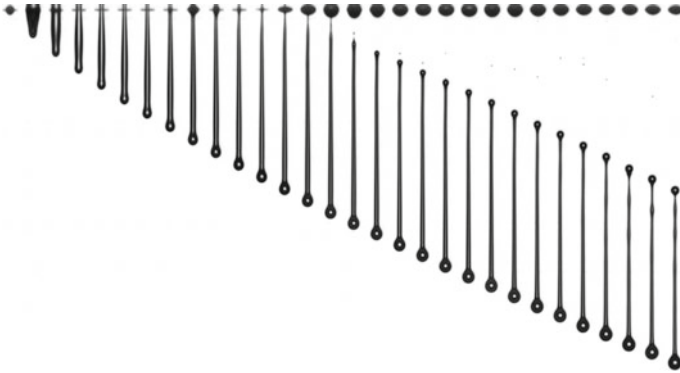
Fig. 2 Stroboscopic imaging of drop-on-demand inkjet droplets using illumination by laser-induced fluorescence (iLIF) [12]. Each image corresponds to a different droplet imaged in a subsequent cycle with a small running delay. The excellent reproducibility of inkjet printing allows to capture the high-speed droplet dynamics in flight at high resolution

experimental approach was used to capture two detailed images of the very same droplet with a small time delay. The obtained velocity profiles were compared to a numerical simulation based on the slender jet approximation of the Navier-Stokes equation and a very good agreement with the model was found [13]. Despite the high optical quality of these images, there are transients or sudden events to which stroboscopic imaging cannot be applied, e.g. to study the details of the breakup of a secondary tail, where we need ultra high-speed imaging in an operating regime exceeding 10 Mfps.

2.2 Rotating Mirror Cameras

Rotating mirror cameras do not suffer from the drawbacks of beam splitting or image intensifying and offer a higher resolution, dynamic range, and frame count. A short exposure time is obtained by sweeping the image during the rapid rotation of a turbine-driven mirror across a photographic film mounted on an arc [14]. The original concepts were devised in the late 1930s and the first camera dates back to the first hydrogen bomb explosion in 1952, see Fig. 3. The high rotation speed of the mirror allows up to 130 frames to be recorded at a maximum frame rate of 25 Mfps. Photographic films offer excellent image quality, however, they have some disadvantages. They have limited light sensitivity, reduced flexibility due to film handling and long turnover time due to film development and processing time. In addition, highly specialized shutters, which are both expensive and inconvenient to use, are required at high speeds to prevent multiple exposure of the film.
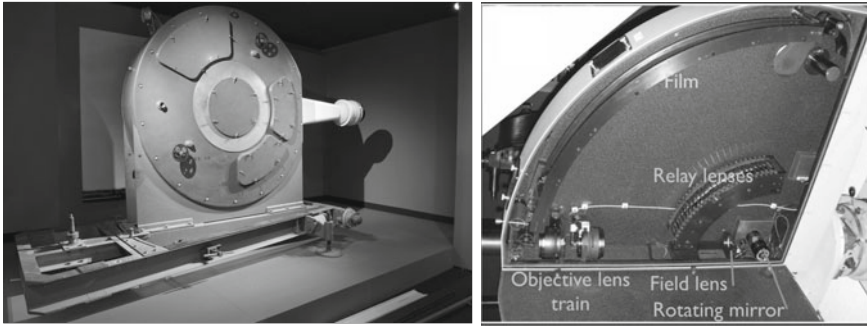
Fig. 3 Rotating mirror cameras have been around since the 1950s. *Left* The C4 rotating mirror high speed camera was developed at the end of World War II to study explosive reactions at the British Atomic Weapons Research Establishment (AWRE)—now exhibited at London's Science Museum. (Reprint permitted by the Science Museum.) *Right* Inside of rotating mirror framing camera with rotating mirror turbine in the lower right corner and the film track spanning the inside of the quarter arc
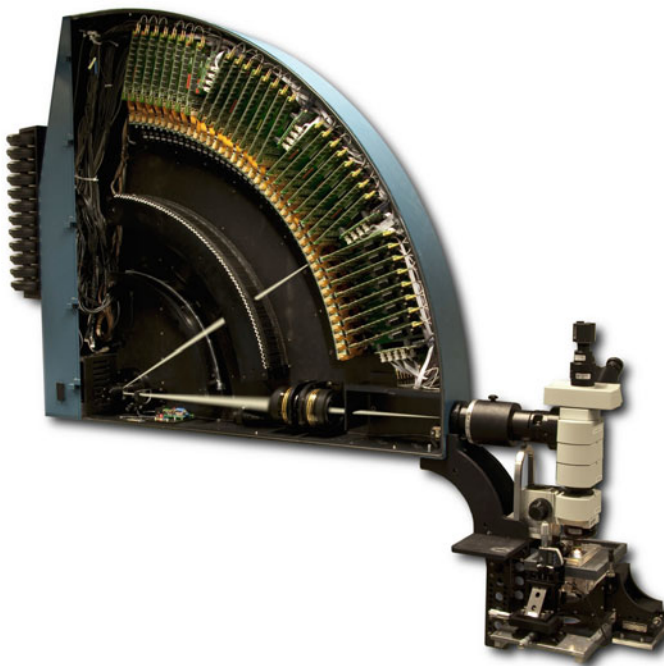
3   Brandaris 128

In a novel concept of the rotating mirror camera introduced in 2003 by Chin et al. [15], a series of CCD sensors replace the traditional negative film thereby greatly improving the sensitivity. Moreover, CCD sensors are highly flexible, can be accurately timed, and allow for multiple and repetitive exposures in short succession. The Brandaris 128 camera [15, 16] is equipped with 128 CCD sensors, each of which can store six full-frame images in its onboard RAM. The helium-driven turbine can rotate at 20,000 rps, completing a sweep across the image arc in just 5 μs, thereby providing an interframe time of 40 ns. The Brandaris 128 camera can therefore acquire a total of 768 frames at a frame rate of 25 Mfps in a set of 6×128 frames, and in its segmented mode it acquires 12×64 frames, or 24×32 frames, or any permutation of the above, provided that a 20-ms readout time is allowed once all 128 channels are filled.

The Brandaris 128 camera has been dedicated predominantly to the study of medical ultrasound contrast agents. The understanding of the interaction of the bubbles and ultrasound has allowed improvement of their performance for which a detailed insight of the microbubble dynamics proved essential. Despite the numerous novel scientific results obtained with the Brandaris 128 camera, until recently the camera still had a few limitations. A few modifications to the camera design in 2012 improved the imaging capabilities, notably a region of interest mode (ROI), a higher number of collected frames (now 16,000) and ultra high-speed fluorescence capabilities [16]. Another ultra high-speed imaging system, named UPMC Cam, based on identical rotating mirror technology was recently introduced with a special emphasis on in vitro and in vivo fluorescence imaging where photon availability is limited and high sensitivity is required [17].

Brandaris 128, illustrated in Fig. 4, is developed from the Cordin 119 (Cordin Company, Salt Lake City, Utah) camera frame. The system combines the superior flexibility and sensitivity of electronic CCD detectors with the high frame rate and high number of frames available in rotating mirror cameras. In front of the camera a variety of lenses can be mounted to suit the need of the experiment, as an example Fig. 4 shows the Brandaris camera equipped with a high-resolution microscope. Other objectives, such as long working distance microscopes and video camera lenses, have also been used. Generally, a suitable field lens is needed to couple such objective lenses to the Brandaris camera and to reduce light loss due to unmatched numerical apertures, which is a particular problem when using high-magnification microscope objectives.

Once an image is formed at the entrance plane of the camera, or primary image plane (Fig. 5), a set of relay lenses projects the target image onto a three-faced mirror prism. The high-speed turbine (Cordin Company Model 1220) is driven by high-pressure bottled helium. The maximum turbine rotation speed is 20,000 rps, or 1.2 million rpm, resulting in a maximum frame rate of 25 Mfps. The gas flow is controlled by a mass flow controller (MFC), which in turn is controlled by a PC. The frame rate and timing parameters are set by internal software, the MFC actively

Fig. 4 The Brandaris 128 ultra high-speed camera equipped with a high-resolution microscope. Inside the camera the film track is replaced by 128 high-sensitivity CCDs. The height of the camera is 1.5 m [1], with permission of Springer
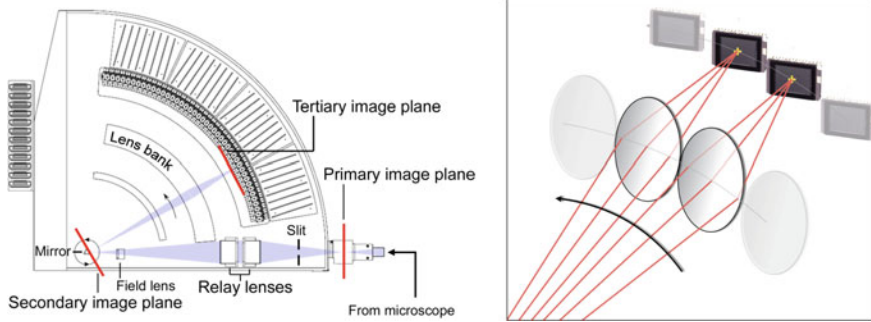
Fig. 5 Optical configuration of the Brandaris 128 camera. *Left* locations of primary, secondary and tertiary image planes. *Right* ray tracing helps to understand why images are stagnant at the sensor plane while the image that is reflected from the rotating mirror is swept across the lens bank

regulates the flow rate between 1 and 100 m^3/h. The active control is needed as the rotation speed and helium flow rate are coupled by a nonlinear relation due to fluid dynamical drag of the mirror assembly in the helium environment, which is the main reason for using helium in the first place; the drag in air would limit the turbine speed to 5000 rps. The response of the turbine also changes over time due to wear and tear on the turbine ball bearings system. The speed of the turbine is monitored by an infrared laser–photodiode pair mounted at 30° below the optical axis. It generates three mirror pulses per prism rotation and these provide accurate timing of the rotation rate. The internal software also utilizes the mirror pulses as a master to control the experiment including the timing of the CCDs and the illumination sources. The field lens in Fig. 5(left) is shifted to either of two preset positions in order to compensate for the change in reflective index while operating in different gases (air or helium).

3.1 Optical Configuration and Miller Principle

Figure 5 shows the optical path upon reflection from the secondary image plane at the rotating mirror. The image passes through an optical lens bank system containing spherical lens pairs (to control focus and magnification) that project the image onto the tertiary and final image plane where the sensors are located. To comply with the small pitch in the arc of the lens bank, the lenses are cut to a narrow slice with a width of 9 mm. The total magnification factor from the primary image plane to the final image arc is 0.44.

The unique optical feature and working principle of the camera is contained in this fine piece of optics and is based on the Miller principle for high-speed cinematography [18, 19]. While the reflected image is swept along the lenses of the lens bank, the image formed in the sensor plane is static and does not move for the

duration of the exposure before it moves to next frame location. This can be understood from simple geometrical optics, if we consider rays emanating from the mirror to sweep across the lenses, as depicted in Fig. 5(right). The ray that passes through the center of the lens is projected at a specific location (that of the center of the CCD). Rays that hit the lens before and after that center position are focused at the very same location, as this is dictated by the positioning of the lenses in the lens bank to project the image in the secondary plane at the mirror surface to the final image plane. Thus, if these rays (and in the bigger picture the conjugated image) are scanned at high-speed, the focused rays (or the projected image) do not move but remains stationary, and long enough to expose the CCD sensors. Ignoring for the moment any change of the dynamic picture due to the high-speed event under study, the image experiences a small residual change as the mirror rotates. This leads to a small deterioration of the image, termed residual mirror drag [14], which is of the order of a few micrometer. The typical drag is calculated to be smaller than the pixel size of the CCD detectors and as a matter of fact smaller than the overall optical resolution of the system using a fixed mirror.

Figure 6(left) illustrates an alternative view of the Miller principle based on the conjugated image in the Fourier plane of the optical system. When the conjugated image is scanned across the aperture of the focusing lens pairs in the lens bank, the sweeping motion is filtered out by the inverse Fourier transform, and the image slowly builds up in amplitude (light intensity) and in resolution, as more complex phase information is gathered within the aperture of the channel. This system then also dictates the triangular illumination profile at the final image plane, see Fig. 6 (right). Here two fast photodiodes mounted in the sensor plane measure the time evolution of the image brightness. It is seen that the triangular profiles [20] overlap between frames, however when the 10–90% integrated illumination intensity is evaluated [15], it was found that the exposure time ($t_{90} - t_{10}$) perfectly fits the
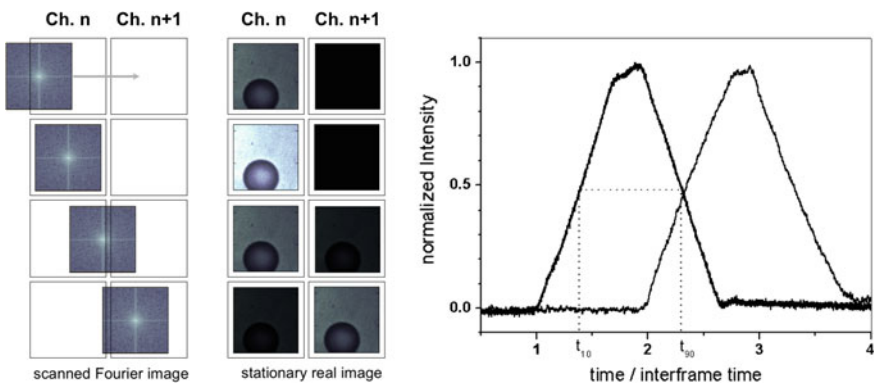
Fig. 6 The Miller principle, which is the key optical feature of rotating mirror cameras, can be understood from scanning the conjugated Fourier transformed image across the apertures at the lens bank position. By inverse Fourier transform at the sensor plane the build up of the real image and it intensity profile is recovered, reprinted from [15], with the permission of AIP Publishing

interframe time (1/frame rate), which in turn is directly defined by the channel pitch. Figure 6(right) also shows that each individual frame is indeed recorded discretely in time, as the intensity level at which t_{10} and t_{90} occur coincides with the crossing of the intensity profiles of the two channels.

3.2   CCD Camera Technology

The images are recorded on 128 un-intensified high-sensitivity CCDs (ICX055AL, Sony Corp., Tokyo, Japan) mounted on an image arc in the final image plane of the camera. Thirty-two CCD Controller Cards, named C^3, built around a microcontroller chip control the CCDs. Each C^3 performs the following tasks: flush and charge transfer of 4 CCDs, readout of the CCDs; storage of the data into a RAM buffer, and command and data input/output, in particular transfer the images to a PC for storage through eight USB 2.0 hubs. Three hardware signal inputs, start, flush, and transfer, provide synchronization to all the C^3 with 40 ns precision. The C^3 s host a memory buffer to accommodate six full recordings. The CCD camera modules measure 27 mm × 40 mm and since the channel pitch at the final image plane is only 9 mm, a surface mirror block assembly was designed to accommodate 3 CCD sensors, one mounted on the optical axis image arc (no mirror required), one mounted on a top plane perpendicular to the original image plane and one mounted on a bottom plane also perpendicular to the original image plane.

The CCD sensor contains 500 × 584 photosensitive cells, each measuring 9 μm × 6 μm. The CCD are read out by a standard flush and charge transfer capture protocol. There is one transport channel for two photosensitive cells, resulting in 500 × 292 effective pixels. The readout of the transport channel is performed by analogue-to-digital conversion. Beginning and end of exposure are therefore in principle defined by flush and charge transfer, respectively. Flush and charge transfer are performed on all pixels in parallel and requires a few microseconds. Readout is performed sequentially on a pixel by pixel basis and requires 20 ms to complete.

Mirror pulses are extracted from the rotating turbine assembly and since the turbine operates at a stable rotation rate for a set value of the mass flow, pretriggers can be derived. From the mirror pulse, flush and transfer pulses are derived for the C^3 s. Moreover, the mirror pulse is used to calculate pre and post-triggers for illumination, wave form generators, switches and multiplexers.

Figure 7(top) shows the standard timing diagram for a Brandaris experiment. Here a single event is captured in a full sequence of 128 frames. Synchronized exposure of the CCDs is ensured by letting the C^3 s perform a flush and charge transfer (xfer) when triggered by the master trigger, typically coupled to the mirror trigger. All CCDs are flushed before channel 1 is illuminated, and a charge transfer is performed right after channel 128 is illuminated. Lead and trail times are ten and a few microseconds, respectively. Charge transfer prevents multiple exposures of the CCD. A readout is performed after charge transfer.
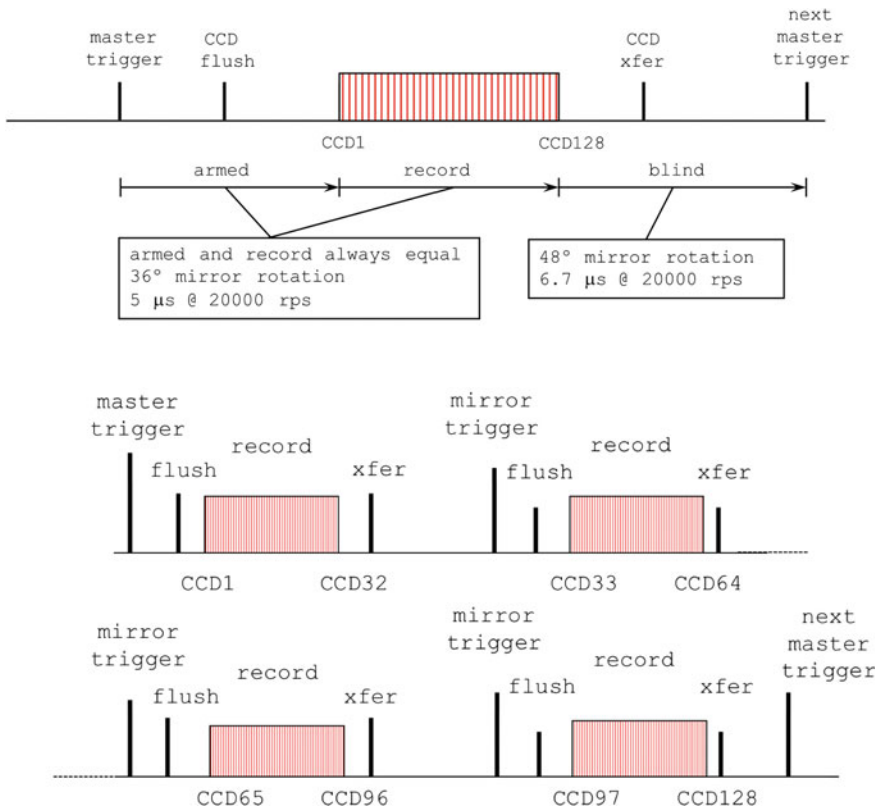
Fig. 7 Brandaris 128 timing diagram. *Top* standard experiment with a single acquisition of 128 frames. *Bottom* segmented mode acquiring 4 segments of 32 frames

The readout time of 20 ms severely limits the speed at which experiments can be repeated. Higher repetition rates are achieved through the use of a segmented mode, see Fig. 7(bottom). In this example, the experiment is designed to capture 4 series of 32 consecutive frames in four mirror periods. During the first mirror period, the C^3 s flush all the CCDs before illumination and charge transfer channels 1–32 after illumination. During a subsequent mirror period, e.g. at the next mirror face, the C^3 s again flush all the CCDs before exposure and then charge transfer channels 33–64 after illumination. As before, the images stored in the CCD transport channels of channels 1–32 are not affected by subsequent illuminations, nor by repetitive flushes after charge transfer.

After acquisition, image frames are realigned using affine transformations to correct for the misalignment between the detector channels, which arise from imperfect positioning of the relay lenses and CCDs (order 50 μm). The transformation matrix is calculated by analyzing the recording of a calibration grid target, to correct for $x - y$ translation, rotation, magnification and perspective.

3.3 Fluorescence Imaging

The Brandaris 128 camera system, as well as the UPMC Cam, host the capability to perform fluorescence microscopy on nanoseconds timescale. To assess the feasibility for high-speed fluorescence imaging a thorough analysis was made, taking into account all parts that contribute to obtain an acceptable signal-to-noise ratio at 25 Mfps: the image sensor, the imaging optics, the fluorescent dye and the excitation light source. The original CCD sensors were found to outperform any new technologies, including back-illuminated CCD's with a factor 2 higher quantum efficiency, and EMCCDs that use electron multiplication which may introduce higher signal levels at the expense of higher noise levels. Optimization of the optical configuration, e.g. by improving the limited numerical aperture within the camera frame, or redesign of the channel pitch left little room for improvement, which means that an increase in sensitivity must come from the fluorescence emission alone. Brighter fluorescence emission means a stronger excitation, and the use of more efficient fluorophores, with increased saturation levels where the photon flux becomes independent of the excitation intensity. It was shown [16, 17] that the fluorescence of microparticles and oil-filled polymeric microcapsules can be imaged successfully at frame rates exceeding 20 Mfps, while microbubbles with a less efficient loading of fluorescent dye molecules could be imaged up to 5 Mfps in fluorescence.

Excitation of the fluorophores is best accomplished with pulsed lasers, however, the repetition rate of pulsed lasers is limited (typically 10 Hz, or 40 kHz for a Cu vapor laser), or the laser fluence drops down dramatically at high repetition rate (200 kHz for Nd:YLF lasers). Thus, for ultra high-speed imaging running at 10 Mfps a separate laser cavity would be required for each individual frame to be able to perform fluorescence imaging frame rates exceeding 1 Mfps, see e.g. the 8-frame approach of Ding et al. [21], with major cost per additional channel. CW (continuous-wave) lasers, e.g. diode-pumped solid-state lasers, can be utilized to excite the fluorescent molecules for a prolonged period of time, using accurate exposure control with an acousto-optic modulator (AOM). Care should be taken, however, for proper dye selection, as less efficient fluorophores can induce non-negligible local heating through non-radiative absorption of laser light. The small form factor of these laser allows the mounting of the laser underneath the camera, as shown in Fig. 8. Coupling of the laser light into the optical path of the microscope was accomplished via a dichroic mirror. The beam is passed through a spatial filtering pinhole and expanded to control the spot size at the sample level. A notch filter located above the dichroic mirror filters out any reflected excitation light. The fluorescence emission is then passed on to the Brandaris camera. The dichroic mirror has a 50% transmission of the Xe-flash light for bright-field illumination, which means that bright-field imaging and fluorescence imaging can be performed in a single experiment, or run, of the camera system. Digital delay control give full control over triggers to laser, AOM, and flash illumination, which gives access to alternating bright field and fluorescence imaging or combined
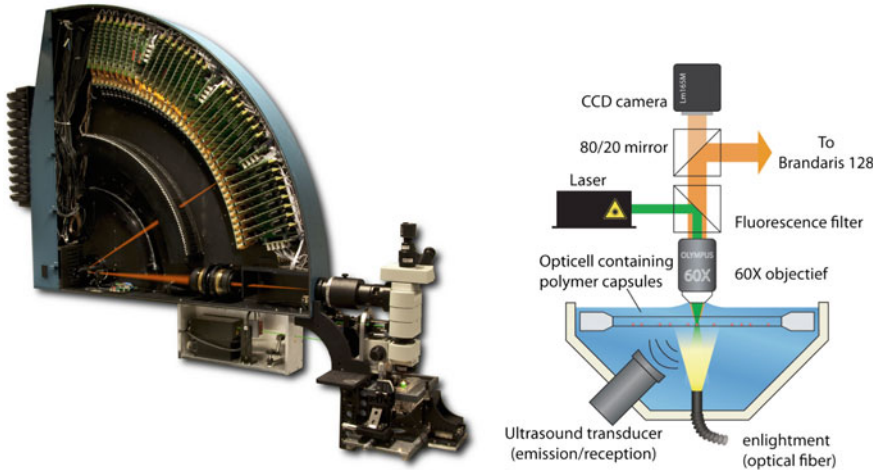
Fig. 8 *Left* Brandaris 128 camera in fluorescence mode, reprinted from[16], with the permission of AIP Publishing. The laser used for illumination is mounted underneath the camera and coupled into the microscope using a dichroic mirror (*right*). Fluorescence is transmitted in the epifluorescent setup and transmitted to the Brandaris camera

recordings where the first 64 frames are recorded in bright field and the second 64 frames are recorded in fluorescence.

3.4 Performance

Optical resolution, image quality and sensitivity of the Brandaris system is governed by the intrinsic f-number of the camera, and the objective lenses used before the primary imaging plane. The combined system was tested using a glass resolution test target with photo-etched lines down to 200 nm separation. At the plane of the image sensor the optical resolution of the camera was 36 line pairs per millimeter horizontally and 16 lp/mm vertically on the image sensor. With a typical magnification for a water-immersion high-resolution microscope objective of $60 \times$ (NA of 0.9) and a $2 \times$ magnifier, and $2.2 \times$ demagnification in the Brandaris, objects as small as 400 nm wide can be clearly defined, see Fig. 9. Optical quality is limited at ultra high speed framing rates by the increased noise level set by the gain of CCD sensor or the image intensifier voltage, in the case of image intensified-CCDs, which, from the start, already present a more grainy image, that only deteriorates for higher gain settings. The un-intensified CCDs in Brandaris 128, that can be used due to the gating function provided by the rotating mirror turbine, help in achieving higher grade optical quality images. For Brandaris the optical sensitivity was expressed in ISO numbers. While quantifying the exact
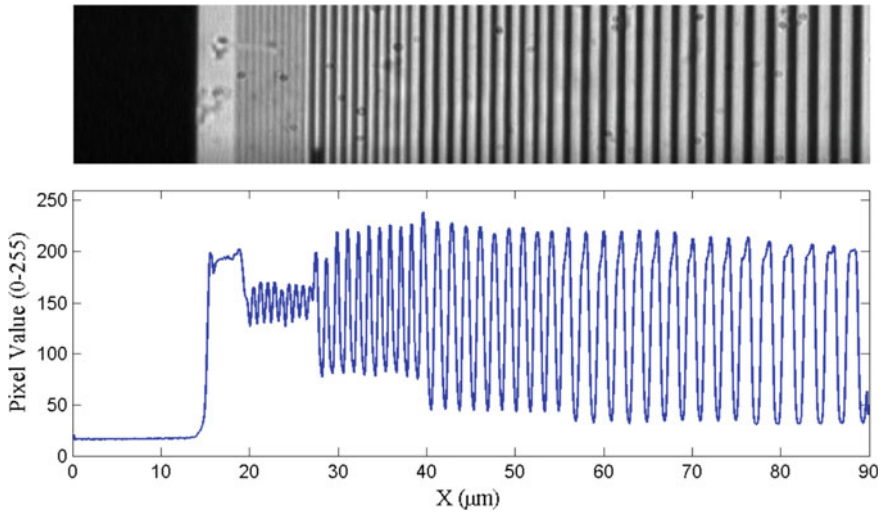
Fig. 9 Resolution measurement of the Brandaris 128 camera using a target grid with a resolution down to 200 nm, reprinted from [15], with the permission of AIP Publishing

ISO number is complex and needs painstaking calibration and a range of spectral illumination boundary conditions, the measured ISO number ranges from 400 to 100,000 depending on the gain setting. Finally, the dynamic range of a camera system is defined as the ratio between the highest light intensity resulting in unsaturated images and the lowest light intensity resulting in detectable images above the noise level. Brandaris 128 gives a near 8-bit dynamic range of 250, but it should be kept in mind that the dynamic range within an image frame is lower than the full dynamic range, since the gain within a single frame is fixed and a typical Brandaris 128 image frame has a dynamic range of 30.

4 Applications

4.1 Microbubble Dynamics

A suspension of ultrasound contrast agents contains a polydisperse size distribution of microbubbles with a size ranging from 1 to 10 μm in diameter. The bubbles resonate when driven near their resonance frequency boosting their radial response. The eigenfrequency of the bubbles follows directly from their size following the Minnaert frequency $f_0 R_0 = 3.3$ μMHz [2, 3], neglecting in first approximation the effect of surface tension and shell elasticity. Thus bubbles of a size of a few micrometer resonate at a driving frequency of a few MHz, right in the heart of the
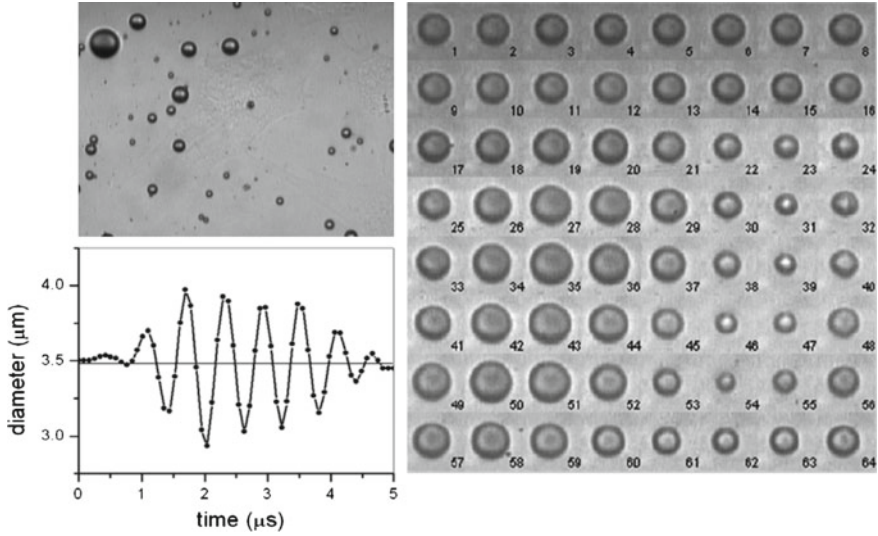
Fig. 10 *Top left* Polydisperse bubbles viewed under the microscope of the Brandaris 128 camera. The corresponding video is available online. *Right* 64 frames of a recoding of an oscillating microbubble, reprinted from N. de Jong et al., Ultrasound Med. Biol. 33 (2007), 653, with the permission of Elsevier. *Bottom left* Radius-time ($R - t$) curve of a single microbubble, reprinted from M. Emmer et al., Ultrasound Med. Biol. 33 (2007), 941, with the permission of Elsevier

medical ultrasound application domain. Figure 10(right) shows 64 frames of the recording of the oscillations of a single microbubble under the microscope taken at 10 Mfps. It nicely shows the transient behavior where the driving kicks in followed by a steady state oscillation of successive expansion and contraction of the microbubble ($\Delta R = 0.30 R_0$) during the insonation with a pulse with six cycles of ultrasound. Analysis of the high-speed recording then allows to plot the size of the bubble as a function of time, giving the radius-time ($R - t$) curve, see Fig. 10 (bottom-right). Note the time scale of 5 μs on the horizontal axis.

The microbubbles are coated with a stabilizing shell to prevent gas loss, dissolution and coalescence of the microbubbles. The bubble dynamics is changed by the addition of a viscoelastic coating, typically consisting of phospholipids [22–25]; shell elasticity increases the stiffness of the system and increases its resonance frequency while shell viscosity increases the damping of the system. Figure 11(top) shows a numerical simulation of this resonance behavior. The uncoated 3.8 μm bubble resonates at 0.85 MHz, nicely following its Minnaert frequency, while the resonance curve of the same bubble coated with a viscoelastic coating has a 40% higher resonance frequency due to shell elasticity and a 5 × wider resonance curve due to shell damping. Here the resonance curves are normalized, but it is obvious that due to damping the amplitude of the coated bubble response decreases by the same amount for the same acoustic energy input.

Fig. 11 *Top* Calculated
resonance curves of uncoated
and coated bubbles of the
same size, reprinted from
[24], with the permission of
AIP Publishing. *Bottom*
Measured resonance curves of
three microbubbles of
different size using the
microbubble spectroscopy
technique, reprinted from [5],
with the permission of AIP
Publishing
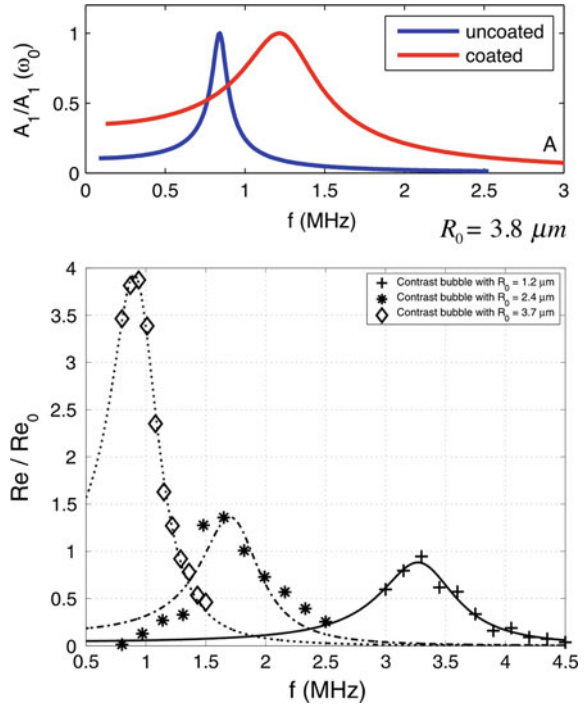
4.2 Non-linear Bubble Dynamics

Experimental validation of bubble shell models that incorporate a physical
description of shell viscoelasticity rely on measurements of the resonance curves of
single bubbles [5, 7]. To this end the response of single microbubbles to a driving
ultrasound pulse is recorded for a range of ultrasound frequencies using Brandaris
in segmented mode. Figure 11(bottom) shows the resonance curves of three sta-
bilized microbubbles with a size of 1.2, 2.4 and 3.7 μm. A fit to the analytical linear
resonance curve is plotted through the 11 maximum amplitude data points that were
recorded in segmented mode running 12 segments of 64 frames (giving 1 ambient
bubble size recoding before ultrasound arrival and 11 well-resolved responses at 11
different frequencies). Shell viscoelastic parameters can then be inferred from a
direct comparison with calculated resonance curves for the uncoated bubble system.
Overvelde et al. [26] operated the Brandaris 128 camera in standard mode to obtain
the response of single microbubbles for 8 different pressures and 12 different fre-
quencies. Using all 128 frames for each exposure requires a total of 16 experiments
which takes approximately half an hour to record. To isolate single bubbles and
keep them positioned in a fixed location for the duration of the experiment, optical
tweezers were developed to trap microbubbles in the dark core of a
Laguerre-Gaussian laser beam [27]. For details, see Chap. 9 (Garbin).

4.3 Laser-Activated Bubbles

In photoacoustic (PA) imaging laser absorption leads to local heating followed by expansion and contraction of the material, which results in the generation of a pressure wave that can be picked up in the far field and transformed into an image. Photoacoustics offers several attractive features in biomedical imaging including excellent spatial resolution and functional information such as blood oxygenation mapping. A key limitation of PA imaging is the penetration depth of the excitation laser, which is limited to tissue depths of 1–2 mm. To address this problem, a number of PA contrast agents have been developed, including dyes (methylene blue, ICG) and metallic nanoparticles. Microbubbles coated with an optically absorbing shell are potentially interesting for contrast-enhanced PA imaging. These bubbles may offer larger signals and have improved biocompatibility over the metallic nanoparticles.

Figure 12(top left) shows a confocal fluorescence image of a microbubble coated with a light-absorbing oil layer. The figure at the bottom left shows nicely how the flurophores are contained in the thin oil layer. Different oils were tested, namely dichloromethane and toluene, that had lower viscosities as compared to that of water. The oil viscosity has a significant influence on the bubble dynamics. The right-most section of Fig. 12 shows the impulse response of the laser-activated bubbles upon single shot 7-ns pulsed laser irradiation recorded with Brandaris 128 in bright-field mode. The middle section shows the $R - t$ curve of the two sets of bubbles and clearly displays the expansion and contraction at the eigenfrequency of the system, which can be used to fully characterize the system. More details of these experiments can be found in [28, 29] and details are also found in Chap. 9 (Stride et al.).

4.4 Bubble Shape Instabilities

Large amplitude bubble oscillations, or what is known as cavitation, can be separated in two different regimes. Inertial cavitation is a synonym of violent dynamics and represents the most chaotic form of microbubble behavior, see [30] and details in Chapter "The Bubble Challenge for High-Speed Photography" (Lauterborn/Kurz). Bubbles driven by ultrasound may also oscillate indefinitely as long as ultrasound is on in a milder regime called stable cavitation. The stability of bubbles lies in the hands of the gas diffusion in and out of the bubble due to surface tension at the gas-liquid interface, of the local dissolved gas concentration in the surrounding liquid (which may be a function of the presence of other dissolving bubbles, known as Ostwald ripening), and of bubble oscillations with changing surface area leading to the process of rectified diffusion. In some special cases a
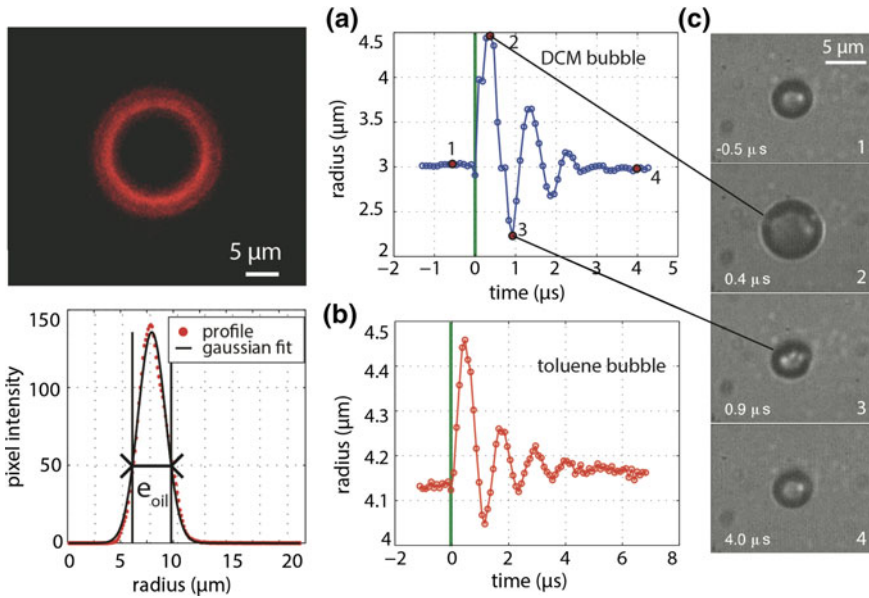
Fig. 12 Ultrafast response of laser-activated bubbles, reprinted from [28, 29], with the permission of AIP Publishing *Top left* confocal image of a light absorbing oil-coated bubble. *Bottom left* Measurement of the oil layer thickness. *Middle R − t* curves demonstrating the impulse response after pulsed laser excitation for a dicholoromethane coated bubble (*top*) and a toluene-coated bubble (*bottom*) demonstrating the effect of different viscosities of the oils. *Right* images taken from a Brandaris 128 recording

small perturbation of the spherical bubble grows as a parametric instability leading to surface mode vibrations and shape instability. These shape modes are associated with a resonance threshold, which can be analyzed following a spherical stability analysis where the mode dynamics is expressed as the solution of a Mathieu equation based on a linearized bubble dynamics equation [31]. Basically we can decompose the bubble dynamics in a volumetric mode and several discrete shape modes ($n = 2 − 6$) that are described by spherical harmonics.

Using ultra high-speed imaging we observed the shape instabilities of bubbles with a size between 10 and 60 μm, see Fig. 13 for an initially spherical 36-μm bubble displaying shape mode oscillations. First, the bubble oscillates in a purely volumetric radial mode, then after 5 cycles of ultrasound the bubble becomes shape-unstable and a surface mode $n = 4$ appears. The bubble was driven by a 10-cycle ultrasound pulse at a frequency of 130 kHz and at a acoustic pressure of 120 kPa. The movie is captured with the Brandaris 128 camera at a frame rate of 1.25 Mfps. Smaller microbubbles display the same physical behavior and shape instability of ultrasound contrast bubbles has been studied in detail by Dollet et al. [32] and by Vos et al. [33].
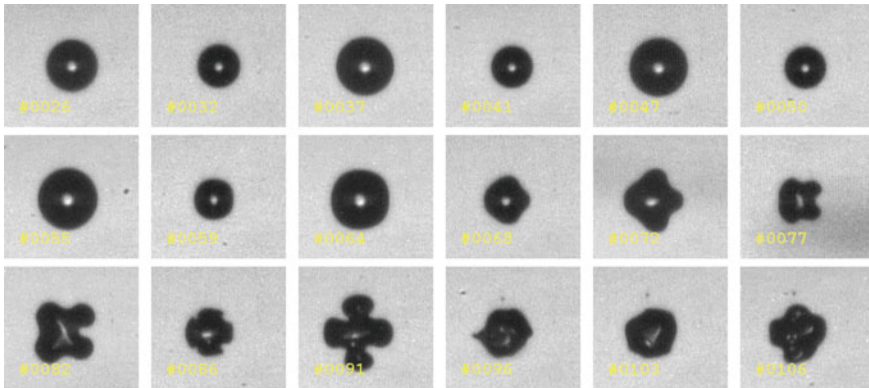
Fig. 13 Microbubble shape oscillations excited through ultrasonic parametric driving [31]. The corresponding video is available online

4.5 Bubble–Cell Interactions

The current challenges of biomedical research revolve around a potent and precise application of the biomechanical effects of targeted agents in acoustics and photoacoustics in order to bring molecular precision and highly localized therapeutic effects to a single cell level [34, 35]. Researchers in academia, as well as in industry, are spending much effort in developing agents that they see as a potential way of addressing the issues of specificity and sensitivity in early diagnostics. Amongst the 'magic bullet' candidates we identify labelled microbubbles that can be decorated with targeting ligands to bind specifically to target cells, and loaded microbubbles covered with nanoparticles, such as liposomes for local drug delivery.

Contrast microbubbles interact with the incoming pressure wave, or laser light. As discussed before, these agents can offer a lot more than contrast generation alone. While the timescale of bubble oscillations is that of microseconds and faster, a number of secondary phenomena occur on the timescale of milliseconds. These include the release of the bubble payload establishment of microstreaming, sonoprinting of functionalized materials onto cell membranes, and sonoporation and the transient disruption of these membranes [36–38]. All these effects are of primordial interest for novel therapies and highly controlled drug and gene delivery, e.g. to treat cancer or a number of genetic diseases more efficiently. This also implies that one needs to follow the subsequent biological processes occurring on a timescale of a few seconds. Following these different processes requires the combination of a range of high-speed imaging techniques [39]. First, the Brandaris 128 camera can be used both in top view and in a non-trivial side view to visualize non-spherical and non-linear features and the dynamics of bubble-induced events. Then, redirecting a fraction of the light towards a high-speed camera operating near 50,000 fps enables the visualization of these secondary effects. The light from two light sources, one pulsed and one continuous wave, are combined for this purpose.

Finally, a highly sensitive CCD camera records the slower events using the remainder of the available light. The spatial resolution of the optical microscope is sufficient to record the bubble oscillations in bright-field, but the fate of the molecules constituting the coating can only be recorded by simultaneous high-speed fluorescence microscopy. A laser is therefore coupled directly into the microscope to excite fluorescently labelled bubbles and their load with a maximum efficiency. Thus, data is collected at microscopic detail at a temporal resolution covering nine orders of magnitude.

The presence of boundaries near oscillating bubbles may pose a concern regarding the applicability of the theoretical predictions and the corresponding experimental observations to the in vivo situation. The in vitro boundary models that neighbor the buoyant bubbles are indeed known to modify significantly their behavior. Alternatively, biological boundaries such as blood vessels or soft tissues found in vivo differ greatly from the in vitro boundaries, and not only by their viscoelastic properties and geometry. In particular, the polymeric membranes that are typically used in most experimental setups, where shown to shift the resonance frequency of the microbubble by as much as 30% [40] and the oscillation amplitude by as much as 40% [27]. Additional results obtained by combining ultra high-speed imaging to advanced manipulation techniques, such as optical tweezers or acoustic radiation forces hint to a complex interaction, depending on the distance of the bubble to the wall and the physical properties of the wall itself which makes such interaction particularly delicate to model. Observations performed in ultra high-speed imaging in side-view, however, reveal how these oscillations can depart from the commonly accepted assumption of bubble sphericity and how the non-spherical character of the oscillation is enhanced by the proximity of a boundary.

Further increase in the insonifying pressure (typically a pressure above 500 kPa for a 3 µm bubble driven at a frequency of 1 MHz) gives rise to a chaotic bubble response. The bubble behavior therefore becomes not only irreproducible but also unpredictable, by definition. In this pressure range, a wide collection of phenomena can be observed, such as jetting [41]. Jetting arises from the inertial collapse of the bubble when the symmetry is broken, e.g. close to a wall or by a gradient of pressure. This particular phenomenon is known to induce damage on supporting structures and is as interesting for cleaning applications as it is concerning for cell toxicity. Ultra high-speed imaging with the Brandaris 128 camera gives direct insight into such phenomena that may also modify the bubble size, either by bubble pinch-off [42], or by gas loss due to changing surfactant concentration and composition. These effects change the acoustic properties of the bubbles and, thus, their response to the acoustic field.

Some biomedical applications require having the agents outside the vasculature, for example to porate or to kill diseased cells beyond the endothelial barrier. One way of achieving this is by injecting nanometer sized agents that are small enough to pass the intercellular spaces in the vessel walls. These agents must then be activated in order to form larger bubbles that can scatter an insonifying ultrasound wave [45, 46]. Many solutions are being investigated, that primarily involve inertial

cavitation and where ultra high-speed imaging provides crucial details on the process at hand. Superheated perfluorocarbon droplets are of particular interest for this application [43, 44, 47]. The strategy here consists in injecting nanodroplets made of volatile perfluorocarbons that can then be vaporized in the target site using ultrasound. An example of an ultra high-speed recording of such acoustic droplet vaporization is given in Fig. 14. Alternatively, one can consider the use of gas entrapping nanoparticles. Mostly polymeric, the nanoparticle structure can offer host nano-sized gas pockets. Upon ultrasound exposure above a certain threshold, that depends upon the particle shape and nature, the nucleus can grow to a size 3 orders of magnitude larger, and emit a strong acoustic response [48].

It is obvious that the contrast agent, once injected, will be brought in contact with cells, before, during and after their activation. Whether they are to be used for
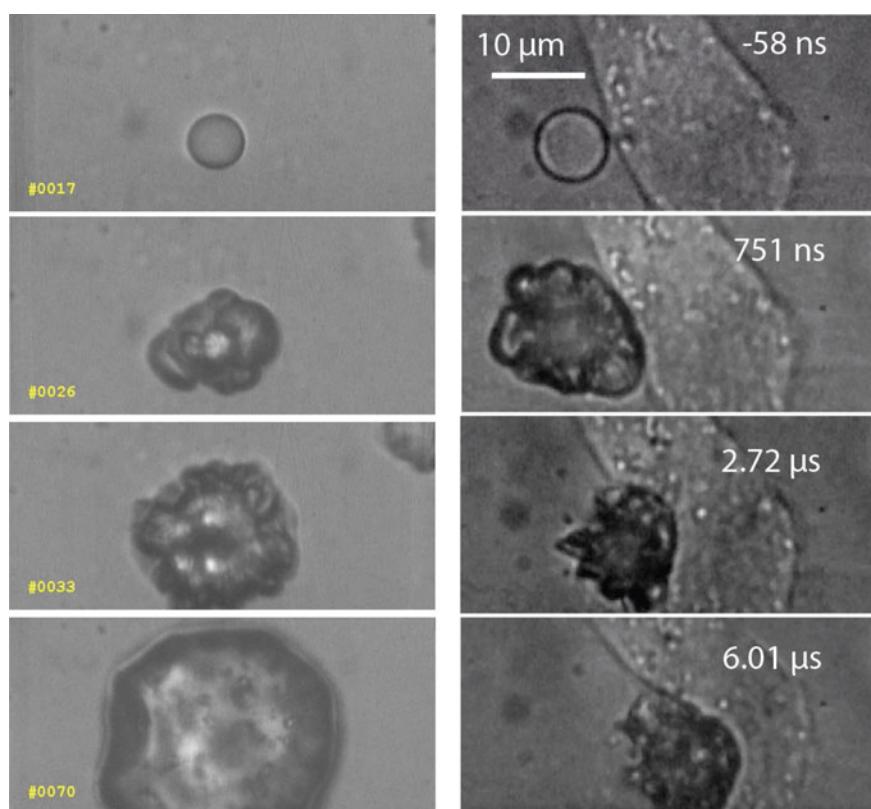
Fig. 14 Acoustic Droplet Vaporization (ADV). *Left* Brandaris 128 recording of the ultrafast vaporization of a 5-µm perfluoropentane (PFP) microdroplet [43]. The corresponding video is available online. *Right* Interaction of a vaporized PFP microdroplet with a neighboring cell. As soon as the droplet is vaporized (by superharmonic focusing [44]) the vapor becomes susceptible to acoustic radiation force and the formed bubble is pushed against the cell (ultrasound from the *left*), reprinted from G. Lajoinie et al., Biomicrofluidics 10 (2016), with the permission of AIP Publishing

therapy of for contrast enhancement, it is crucial to investigate the resulting inter-action. Here again, only a combination of both ultra high-speed bright-field imaging and fluorescence microscopy can provide simultaneous information of the cell structure and functions, and on the bubble size and location. Generally, biological events also occur on longer timescales. The closure dynamics of pores for example occurs over the timescale of a second. Therefore, a successful optical observation of, for example, cell response to a bubble-induced mechanical stimulus also requires to combine fluorescence and bright-field high-speed microscopy for accessing simultaneously the long term bubble behavior and molecular information. Ultra high-speed imaging further provides complete and crucial information on the bubble behavior on a nanosecond timescale.

An example of nanosecond bubble dynamics related to cell biological response to the stress induced by US-activated microbubbles is presented in Fig. 15. Here, bubbles loaded with fluorescent nanospheres are introduced near cells cultured on a CLINIcell membrane. The seconds timescale confocal image (bottom left) shows fluorescently labeled microbubbles (green) and fluorescently labelled cells (Cell
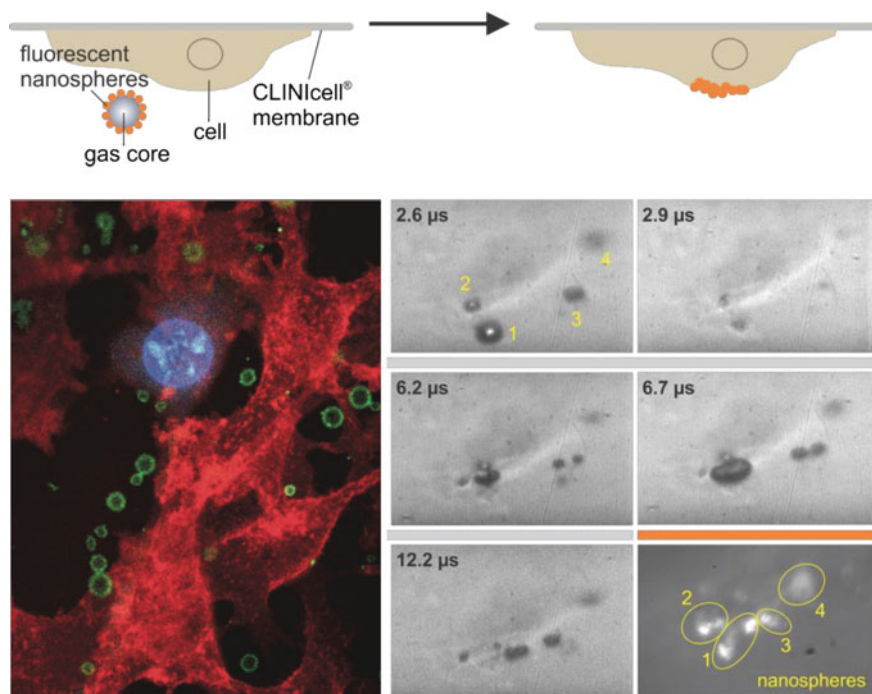
Fig. 15 Bubble-cell interactions are studied in a flow cell (*top*) where bubbles are introduced near a cell monolayer. Activation of the loaded microbubbles with ultrasound leads to deposition of the load onto the cell (sonoprinting [39]). *Bottom left* Confocal fluorescence image of cells (*red*) and bubbles (*green*), with the transfected cell nucleus in blue. *Bottom right* Brandaris 128 recording of the associated bubble dynamics at the nanoseconds timescale

mask Red) and where one cell has been porated (cytox blue). The bottom-right picture shows ultra high-speed imaging of the microbubble oscillations that lead to nanosphere release (nanosphere-loaded microbubbles, side view). Bright-field imaging was performed with the Brandaris 128 camera, operating at a frame rate of 10.5 Mfps. An ultrasound pulse of 100 cycles and a pressure of 300 kPa was sent and the first 12 μs of the experiment were recorded. A fluorescence image was acquired before and after bright-field imaging. The microbubbles are observed to exhibit non-spherical oscillations with repeated gas core coalescence and fragmentation, while acoustic radiation forces translate them towards and along the CLINIcell membrane. The fluorescence images show the localization of the fluorescent nanospheres, and indicate that the microbubbles release and deposit their nanospheres during microbubble activation, termed sonoprinting, as sketched in the top cartoon.

4.6 Diminutive Microjets

A narrow size distribution in droplet formation is important in many industrial and medical applications. For example, in inkjet printing monodisperse microdroplets are needed to accurately control impact and deposition on the target substrate. In pulmonary drug delivery a narrow size distribution of microdroplets is highly advantegeous for optimal drug delivery, as too large droplets are deposited on the trachea, while smaller droplets are inhaled, then exhaled again, or are lost by evaporation. Thus, only droplets of a size around 3 μm reach the deepest alveoli and target the disease.

Monodisperse microspray atomization can be achieved efficiently by Rayleigh breakup of a diminutive microjet produced in a 1-μm nozzle [49]. The jet breaks up into droplets due to the interfacial capillary forces [50, 51] and the droplets produced have a diameter that is exactly 1.89 × the jet diameter. The corresponding capillary breakup time $\tau_b = \sqrt{\rho_w r_j^3 / \sigma_w}$. With a jet radius of 1.25 μm, a density of 1000 kg/m^3, and a surface tension σ_w of 72 mN/m we find τ_b = 160 ns. If we obey the minimum Nyquist condition we need to image at a frame rate of at least 12 Mfps. Figure 16 shows the breakup of such a liquid jet into microdroplets, taken at a frame rate of 13.76 Mfps, and indeed barely fulfilling the criterion. These results of ultra high-speed imaging contributed to the validation of one and two-dimensional numerical models that were developed for diminutive Rayleigh jets.

4.7 Drop-On-Demand Inkjet Printing

Drop formation in inkjet printing is an almost perfectly reproducible process, and single-flash photography is frequently applied to its visualization [13, 52–54]. For
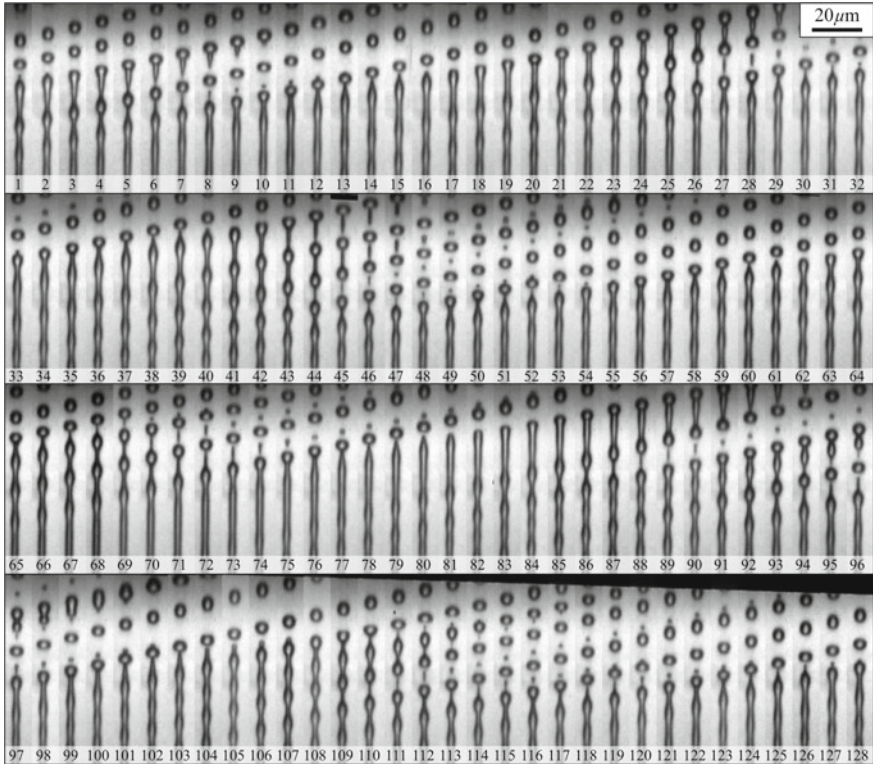
Fig. 16 Atomization following droplet breakup of a 1-μm radius micronozzle jet taken with the Brandaris 128 camera near 14 Mfps, reprinted from [49], with the permission of AIP Publishing

non-reproducible transients that cannot be captured with stroboscopic imaging we resort to real-time imaging with the Brandaris 128 camera. Figure 17 shows the formation of a pL droplet at a drop-on-demand frequency 50 kHz. Special emphasis is put on the breakup of the tail from the meniscus. Figure 17(bottom) shows the formation of a secondary tail (bottom left) that breaks up and forms a series of satellite droplets (bottom middle, right) with a volume of less than 50 fL. Preventing the formation of these satellite droplets is of utmost importance for print quality and for the reduction of aerosol contamination in inkjet machines. The physical insight in the breakup mechanism provided by the Brandaris 128 camera can lead to further optimization in a variety of nanotechnology applications.
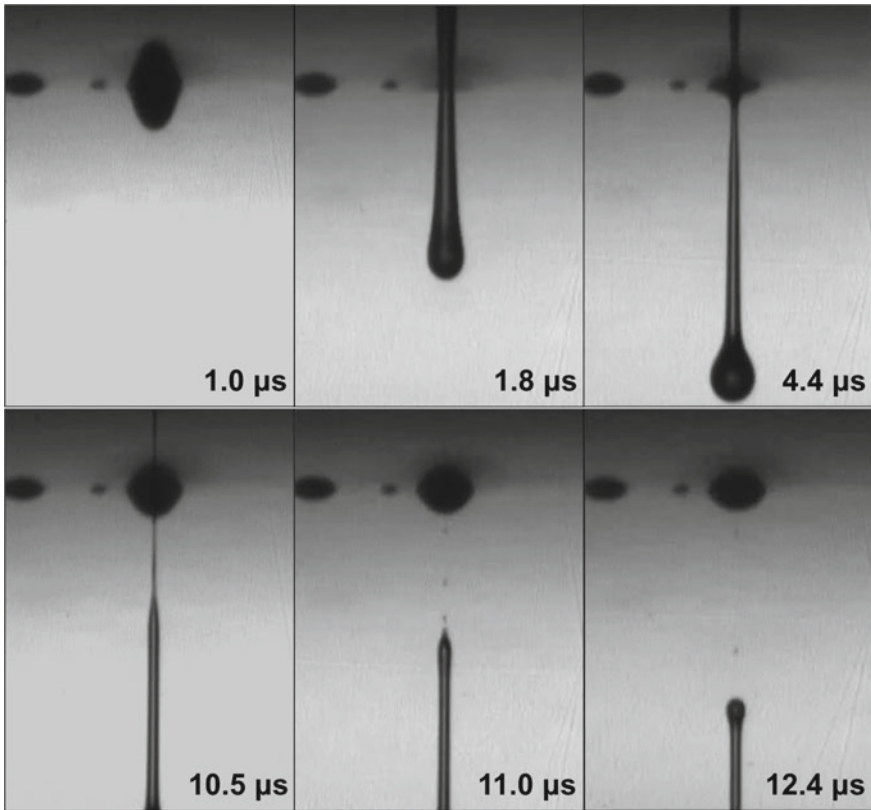
Fig. 17 Inkjet droplet formation imaged with the Brandaris 128 camera at 10 Mfps. Focus is put on the breakup of the secondary tail that connects the primary tail of the droplet with the meniscus. Reduction of satellite droplet formation after breakup improves print quality and reduces aerosol contamination

5 Conclusions

The Brandaris 128 camera has been a unique ultra high-speed imaging system, ever since its introduction in 2003. Various improvements were made in the last decade to further contribute to the versatility of the system, including a faster segmented mode, a region of interest mode boosting the number of acquisition frames to 16,000, the addition of optical tweezers, and the option to capture images in fluorescence, even combined with bright-field imaging. The reduction of the time between separate recordings has been reduced by three orders of magnitude from 80 ms initially to 17 µs now, enabling imaging at multiple timescales ranging from nanoseconds to milliseconds. Combined with its maximum frame rate of 25 Mfps, the Brandaris 128 remains an exceptional camera with great potential for future research both in medical imaging and in nanotechnology industry.

References

1. M. Versluis, High-speed imaging in fluids. Exp. Fluids **54**, 1–35 (2013)
2. M. Mennaert, On musical air-bubbles and the sounds of running water. Phil. Mag. **16**, 235–248 (1933)
3. T.G. Leighton, *The Acoustic Bubble* (Academic Press, London, 1994), p. 306
4. P.N. Burns, D. Hope Simpson, M.A. Averkiou, Nonlinear imaging. Ultrasound Med. Biol. **26**, S19–S22 (2000)
5. S.M. van der Meer, B. Dollet, C.T. Chin, A. Bouakaz, M. Voormolen, N. de Jong, M. Versluis, D. Lohse, Microbubble spectroscopy of ultrasound contrast agents. J. Acoust. Soc. Am. **128**, 648–656 (2007)
6. J. Sijl, B. Dollet, M. Overvelde, V. Garbin, T. Rozendal, N. de Jong, D. Lohse, M. Versluis, Subharmonic behavior of phospholipid-coated ultrasound contrast agent microbubbles. J. Acoust. Soc. Am. **128**, 3239–3252 (2010)
7. T. Faez, M. Emmer, M. Docter, J. Sijl, M. Versluis, N. de Jong, Characterizing the subharmonic response of phospholipid-coated microbubble for carotid imaging. Ultrasound Med. Biol. **37**, 958–970 (2011)
8. E. Muybridge, AV. Mozley, in *Human and Animal Locomotion* (Dover, New York, 1887)
9. B. Brixner, J.M. Dewey, R.G. Racca (Eds.), in *20th International Congress on High Speed Photography and Photonics, Proceedings* (SPIE, Bellingham, 1992), vol. 1801, pp. 52–60
10. J. Honour, in *21st International Congress on High Speed Photography and Photonics, Proceedings* (SPIE, Bellingham, 1994), vol. 2513, pp. 28–33
11. B.R. Lawrence, Review of ULTRANAC high-speed camera: applications, results, and techniques. Proc. SPIE **2869**, 882–887 (1997)
12. A. van der Bos, A. Zijlstra, E. Gelderblom, M. Versluis, iLIF: illumination by laser-induced fluorescence for single flash imaging on a nanoseconds timescale. Exp. Fluids **51**, 1283–1289 (2011)
13. A. van der Bos, M.J. van der Meulen, T. Driessen, M. van den Berg, H. Reinten, H. Wijshoff, M. Versluis, D. Lohse, Velocity profile inside piezoacoustic inkjet droplets in flight: comparison between experiment and numerical simulation. Phys. Rev. Appl. **1**, 014004 (2014)
14. E.A. Igel, M. Kristiansen, *Rotating-mirror streak and framing cameras*, vol. PM43 (SPIE, Bellingham, 1997)
15. C.T. Chin, C. Lancée, J. Borsboom, F. Mastik, M.E. Frijlink, N. de Jong, M. Versluis, D. Lohse, Brandaris 128: a digital 25 million frames per second camera with 128 highly sensitive frames. Rev. Sci. Instr. **74**, 5026–5034 (2003)
16. E. Gelderblom, R. Vos, F. Mastik, T. Faez, T. Kokhuis, T. van der Steen, N. de Jong, D. Lohse, M. Versluis, Brandaris 128 ultra-high-speed imaging facility: 10 years of operation, updates and enhanced features. Rev. Sci. Instr. **83**, 103706 (2012)

17. X. Chen, J. Wang, M. Versluis, N. de Jong, F.S. Villanueva, Ultra-fast bright field and fluorescence imaging of the dynamics of micrometer-sized objects. Rev. Scie. Instr. **84**, 063701 (2013)
18. C.D. Miller, Half-million stationary images per second with refocused revolving beams. J. Soc. Motions Pic. Eng. **53**, 479–488 (1949)
19. V. Parker, C. Roberts, Rotating mirror and drum cameras, in *High Speed Photography and Photonics*, ed. by S.F. Ray (SPIE, Bellingham, 2002), pp. 167–180
20. A. Skinner, Versatile high speed rotating mirror cameras. J. Sci. Instrum. **39**, 336–343 (1962)
21. T. Ding, T.H. van der Meer, M. Versluis, M. Golombok, J. Hult, M. Aldén, C.F. Kaminski, Time-resolved PLIF measurements in turbulent diffusion flames, in *Third International Symposium on Turbulence, Heat and Mass Transfer, Proceedings*, ed. by Y. Nagano, K. Hanjalic, T. Tsuji (2000) pp. 857–864
22. P. Marmottant, S.M. van der Meer, M. Emmer, M. Versluis, N. de Jong, S. Hilgenfeldt, D. Lohse, A model for large amplitude oscillations of coated bubbles accounting for buckling and rupture. J. Acoutst. Soc. Am. **118**, 3499–3505 (2005)
23. N. de Jong, M. Emmer, A. van Wamel, M. Versluis, Ultrasonic characterization of ultrasound contrast agents. Med. Biol. Eng. Comput. **47**, 861–873 (2009)
24. J. Sijl, M.L.J. Overvelde, B. Dollet, V. Garbin, N. de Jong, D. Lohse, M. Versluis, "Compression-only" behavior: A second-order nonlinear response of ultrasound contrast agent microbubbles. J. Acoust. Soc. Am. **129**, 1729–1739 (2011)
25. T. Faez, M. Emmer, K. Kooiman, M. Versluis, A.F.W. van der Steen, N. de Jong, 20 years of ultrasound contrast agent modeling. IEEE Trans. Ultrason. Ferroelec. Freq. Contri. **60**, 6–20 (2013)
26. M.L.J. Overvelde, V. Garbin, J. Sijl, B. Dollet, N. de Jong, D. Lohse, M. Versluis, Nonlinear shell behavior of phospholipid-coated microbubbles. Ultrasound Med. Biol. **36**, 2080–2092 (2010)
27. V. Garbin, D. Cojoc, E. Ferrari, E. di Fabrizio, M.L.J. Overvelde, S.M. van der Meer, N. de Jong, D. Lohse, M. Versluis, Changes in microbubble dynamics near a boundary revealed by combined optical micromanipulation and high-speed imaging. Appl. Phys. Lett. **90**, 114103 (2007)
28. G. Lajoinie, E. Linnartz, P. Kruizinga, N. de Jong, E. Stride, G. van Soest, M. Versluis, Laser-driven resonance of dye-doped oil-coated microbubbles: A theoretical and numerical study. J. Acoust. Soc. Am. **141**, 2727–2745 (2017)
29. G. Lajoinie, J.-Y. Lee, J. Owen, P. Kruizinga, N. de Jong, G. van Soest, E. Stride, M. Versluis, Laser-driven resonance of dye-doped oil-coated microbubbles: experimental study, J. Acoust. Soc. Am. (in print) (2017)
30. W. Lauterborn, Kavitation durch Laserlicht (Laser-induced cavitation). Acustica **31**, 51–78 (1974)
31. M. Versluis, P. Palanchon, D.E. Goertz, I. Heitman, S.M. van der Meer, B. Dollet, N. de Jong, D. Lohse, Microbubble shape oscillations excited through an ultrasound-driven parametric instability. Phys. Rev. E **82**, 026321 (2010)
32. B. Dollet, S.M. van der Meer, V. Garbin, N. de Jong, D. Lohse, M. Versluis, Nonspherical oscillations of ultrasound contrast agent microbubbles. Ultrasound Med. Biol. **34**, 1465–1473 (2008)
33. H.J. Vos, B. Dollet, J.G. Bosch, M. Versluis, N. de Jong, Ultrasound Med. Biol. **34**, 685–688 (2008)
34. I. Lentacker, I. de Cock, R. Deckers, S.C. de Smedt, C.T. Moonen, Understanding ultrasound induced sonoporation: definitions and underlying mechanisms. Adv. Drug Deliv. Rev. **72**, 49–64 (2014)
35. K. Kooiman, H.J. Vos, M. Versluis, N. de Jong, Acoustic behavior of microbubbles and implications for drug delivery. Adv. Drug Deliv. Rev. **72**, 28–48 (2014)
36. A. van Wamel, A. Bouakaz, M. Versluis, N. de Jong, Micromanipulation of endothelial cells: Ultrasound-microbubble-cell interaction. Ultrasound Med. Biol. **30**, 1255–1258 (2004)

37. A. van Wamel, K. Kooiman, M. Harteveld, M. Emmer, F.J. ten Cate, M. Versluis, N. de Jong, Vibrating microbubbles poking individual cells: drug transfer into cells via sonoporation. J. Contr. Rel. **112**, 149–155 (2006)
38. K. Kooiman, M.R. Böhmer, M. Emmer, H.J. Vos, C. Chlon, W.T. Shi, C.S. Hall, S. de Winter, K. Schroen, M. Versluis, N. de Jong, A. van Wamel, Oil-filled polymer microcapsules for ultrasound-mediated delivery of lipophilic drugs. J. Contr. Rel. **133**, 109–118 (2009)
39. I. de Cock, G. Lajoinie, M. Versluis, S.C. de Smedt, I. Lentacker, Sonoprinting and the importance of microbubble loading for the ultrasound mediated cellular delivery of nanoparticles. Biomaterials **83**, 294–307 (2016)
40. M.L.J. Overvelde, V. Garbin, B. Dollet, N. de Jong, D. Lohse, M. Versluis, Dynamics of coated microbubbles adherent to a wall. Ultrasound Med. Biol. **37**, 1500–1508 (2011)
41. C.D. Ohl, M. Arora, R. Ikink, N. de Jong, M. Versluis, M. Delius, D. Lohse, Sonoporation from jetting cavitation bubbles. Biophys. J. **91**, 4285–4295 (2006)
42. H.J. Vos, B. Dollet, M. Versluis, N. de Jong, Nonspherical shape oscillations of coated microbubbles in contact with a wall. Ultrasound Med. Biol. **37**, 935–948 (2011)
43. O. Shpak, T.J.A. Kokhuis, Y. Luan, D. Lohse, N. de Jong, B. Fowlkes, M. Fabiilli, M. Versluis, Ultrafast dynamics of the acoustic vaporization of phase-change microdroplets. J. Acoust. Soc. Am. **134**, 1610–1621 (2013)
44. O. Shpak, M. Verweij, H.J. Vos, N. de Jong, D. Lohse, M. Versluis, Acoustic droplet vaporization is initiated by superharmonic focusing. Proc. Natl. Acad. Sci. **111**, 1697–1702 (2014)
45. N. Reznik, O. Shpak, E.C. Gelderblom, R. Williams, N. de Jong, M. Versluis, P.N. Burns, The efficiency and stability of bubble formation by acoustic vaporization of submicron perfluorocarbon droplets. Ultrasonics **53**, 1368–1376 (2013)
46. N. Reznik, G. Lajoinie, O. Shpak, E.C. Gelderblom, R. Williams, N. de Jong, M. Versluis, P.N. Burns, On the Acoustic Properties of Vaporized Submicron Perfluorocarbon Droplets. Ultrasound Med. Biol. **40**, 1379–1384 (2014)
47. O. Shpak, L. Stricker, M. Versluis, D. Lohse, The role of gas in ultrasonically driven vapor bubble growth. Phys. Med. Biol. **58**, 2523–2535 (2013)
48. J.J. Kwan, G. Lajoinie, N. de Jong, E. Stride, M. Versluis, C.C. Coussios, Ultrahigh-speed dynamics of micrometer-scale inertial cavitation from nanoparticles. Phys. Rev. Appl. **6**, 044004 (2016)
49. W. van Hoeve, S. Gekle, J.H. Snoeijer, M. Versluis, M.P. Brenner, D. Lohse, Breakup of diminutive Rayleigh jets. Phys. Fluids **22**, 122003 (2010)
50. J.A.F. Plateau, *Statique expérimentale et théorique des liquides soumis aux seules forces moléculaires* (Gauthier-Villard, Paris, 1985)
51. L. Rayleigh, On the capillary phenomena of jets. Proc. R. Soc. London **29**, 71–79 (1879)
52. H. Dong, W.W. Carr, J.F. Morris, Rev. Sci. Instr. **77**, 085101 (2006)
53. I.M. Hutchings, G.D. Martin, S.D. Hoath, High speed imaging and analysis of jet and drop formation. J. Imaging Sci. Techn. **51**, 438–444 (2007)
54. D. Cressey, 365 days: images of the year. Nature **516**, 304–309 (2014)